Journal of the Ceramic Society of Japan 126 [10] 743-749 2018
DOI http://doi.org/10.2109/jcersj2.18054

JCS-Japan

FULL PAPER

Phase transitions of Sm_3NbO_7, $(Sm_{1-x}Ln_x)_3NbO_7$ (Ln = Nd, Eu) and Sm_3TaO_7 with fluorite-related structure

Yukio HINATSU[1,†] and Yoshihiro DOI[1]

[1] Division of Chemistry, Graduate School of Science, Hokkaido University, Sapporo 060–0810, Japan

The phase transition of Sm_3NbO_7 with orthorhombic fluorite-related structure was investigated. Three kinds of solid solutions, $Sm_3(Nb_{1-x}Ta_x)O_7$, $(Sm_{1-x}Nd_x)_3NbO_7$, and $(Sm_{1-x}Eu_x)_3NbO_7$ were prepared. Sm_3NbO_7 and Sm_3TaO_7 form complete solid solutions, and their structures are well described with the space group $C222_1$. The phase transition temperature for $Sm_3(Nb_{1-x}Ta_x)O_7$ increases from 1080 K with increasing Ta concentration. Sm_3TaO_7 undergoes the phase transition when the temperature is increased through ca. 1340 K and above the transition temperature, its structure is well described with space group *Pnma*. The phase transition temperature for $(Sm_{1-x}Nd_x)_3NbO_7$ decreases with Nd concentration. On the other hand, that for $(Sm_{1-x}Eu_x)_3NbO_7$ increases with the ratio of Eu concentration. However, both of these solid solutions show the same trend, i.e., with decreasing the average rare earth size, the phase transition temperature of $(Sm_{1-x}Ln_x)_3NbO_7$ (Ln = Nd, Eu) increases. This trend is the same as that for Ln_3MO_7 (M = Mo, Ru, Re, Os, or Ir). That is, the phase transition occurs with lattice contraction.

Key-words : Phase transition, Samarium, Niobium, Oxides, Fluorite-related structure

[Received March 22, 2018; Accepted April 19, 2018]

1. Introduction

Ternary metal oxides of general formula Ln_3MO_7 (Ln is a rare earth element; M is a pentavalent transition element such as Nb, Mo, Ru, Sb, Ta, Re, Os, or Ir) have been attracting great interest, because they exhibit magnetic,[1)–20)] dielectric[21),22)] and photocatalytic activity[23),24)] based on their unique crystal structures. They have an ordered, defect-fluorite superstructure. The relationship to the fluorite structure is as follows. The fluorite unit cell for oxides has the composition $M^{4+}{}_4O_8$. If the four tetravalent metal ions are replaced by three trivalent ions (Ln) and one pentavalent ion (M), one oxide vacancy is formed per fluorite cell. Due to the significant differences in radii between the Ln^{3+} and M^{5+} ions, cation ordering occurs on the metal sites and the oxide-vacancy orders on the anion sites.

In 1979, Rossell first determined the crystal structure of La_3NbO_7.[25)] It was well described in the orthorhombic space group *Cmcm*. The M^{5+} ion is coordinated with six oxygen ions, forming an MO_6 octahedron. These octahedra share corners forming one-dimensional chains which are oriented along the *c*-axis. Although the space group for the La_3NbO_7 now turned out to be *Pnma*,[26)] the structure of many Ln_3MO_7 compounds is well described in the orthorhombic space group *Cmcm*.[1)–17),25),27)–38)] For some compounds such as Ln_3TaO_7 (Ln = Y, Sm–Ho),[32),33),35)] Ln_3SbO_7 (Ln = Sm–Ho)[39),40)] and Ln_3MoO_7 (Ln = La–Nd, Sm, Eu),[18),19),41)–43)] their structures have been described with the space groups $C222_1$, $C222_1$ and $P2_12_12_1$, respectively.

Another topic of Ln_3MO_7 compounds is that detailed magnetic and thermal investigations on the ruthenium-, rhenium-, iridium-, osmium- and molybdenum-containing members of the Ln_3MO_7 family show low-temperature structural phase transitions.[3)–5),7),9),12),13),15),19),29),31),43)]

As for M = Nb compounds, crystal structures and magnetic properties for Ln_3NbO_7 (Ln = La, Pr, Nd, Sm–Lu) were reported.[44)] They have the fluorite-related structures with space group *Pnma* (Ln = La, Pr, Nd), $C222_1$ (Ln = Sm–Tb), or *Fm*-3*m* (Ln = Dy–Lu).

Concerning the phase transition, Klimenko et al. reported that Ln_3NbO_7 (Ln = La, Pr, Nd, Sm, Gd) show phase transitions at relatively high temperatures and that the phase transitions is due to the displacement of atoms with no change in the crystal system and no appreciable change in lattice parameters.[45)] Cai and Nino showed that La, Nd, and Gd compounds undergo a phase transition at 360, 450, and 340 K, respectively and above the phase transition temperature, they transform to the same orthorhombic crystal structures with space group *Cmcm*.[46),47)] The trend of the phase transition temperature against the ionic radius of rare earth for these niobium compounds is quite different from those for Ln_3MO_7 (M = Ru, Os, Re, Ir, Mo) where the phase transition temperature increases

† Corresponding author: Y. Hinatsu; E-mail: hinatsu@sci.hokudai.ac.jp

‡ Preface for this article: DOI http://doi.org/10.2109/jcersj2.126.P10-1

with decreasing Ln ionic radius for any Ln_3MO_7 compounds.[9),12),13),31),43)] It is worth noting that Sm_3NbO_7 undergoes the phase transition at a very high temperature, 1080 K, compared with other Ln_3MO_7 compounds. On the other hand, Eu_3NbO_7 does not show any phase transition up to 1473 K, and the phase transition temperature for Nd_3NbO_7 is 477 K.[48)] In addition, it is reported that no phase transition has been reported for the corresponding tantalum compound, Sm_3TaO_7.

There still exist many points which should be clarified for the high-temperature phase transition of Sm_3NbO_7. In this study, we prepared three kinds of solid solutions; (1) $Sm_3(Nb_{1-x}Ta_x)O_7$, (2) $(Sm_{1-x}Nd_x)_3NbO_7$, and (3) $(Sm_{1-x}Eu_x)_3NbO_7$. Then, we performed high-temperature X-ray diffraction measurements for these solid solutions in addition to their differential thermal analysis (DTA) in order to clarify the phase transition of Sm_3NbO_7 compound.

2. Experimental

2.1 Sample preparation

Polycrystalline samples were prepared by the standard solid state reaction. Reagent grade powders of rare earth oxides (Nd_2O_3, Sm_2O_3, Eu_2O_3), niobium oxides (Nb_2O_5) and tantalum oxides (Ta_2O_5) were used as starting materials. Before use, Nd_2O_3 was dried at 1173 K overnight. These reagents were weighed in an appropriate metal ratio and well mixed in an agate mortar. The mixtures were pressed into pellets and heated in air at 1773 K for 30 h with two interval re-grinding and re-pelletizing. After heating, the samples were cooled down in the furnace.

2.2 X-ray diffraction analysis

Powder X-ray diffraction profiles were measured using a Rigaku Multi-Flex diffractometer with Cu-$K\alpha$ radiation ($\lambda = 1.5406$ Å) equipped with a curved graphite monochromator. The data were collected by step-scanning in the angle range of $10° \leq 2\theta \leq 120°$ at a 2θ step-size of 0.02°. For high-temperature X-ray diffraction measurements, the sample was heated on the Pt plate and the experimental temperature range was from 298 to 1473 K.

The X-ray diffraction data were analyzed by the Rietveld technique, using the programs RIETAN-FP,[49)] and the crystal structure was drawn by using the VESTA program.[50)]

2.3 Differential thermal analysis (DTA) measurements

The DTA measurements were carried out under flowing air atmosphere over the temperature range from 298 to 1500 K using TG–DTA 2000S (Mac Science, Japan). The heating and cooling rate was 5 K/min.

3. Results and discussion

3.1 $Sm_3(Nb_{1-x}Ta_x)O_7$ solid solutions

The crystal structures for Sm_3NbO_7 and Sm_3TaO_7 are well described with both the same space group $C222_1$. The results of X-ray diffraction measurements for $Sm_3(Nb_{1-x}Ta_x)O_7$ ($x = 0.1$, 0.2, —, 0.9) show that

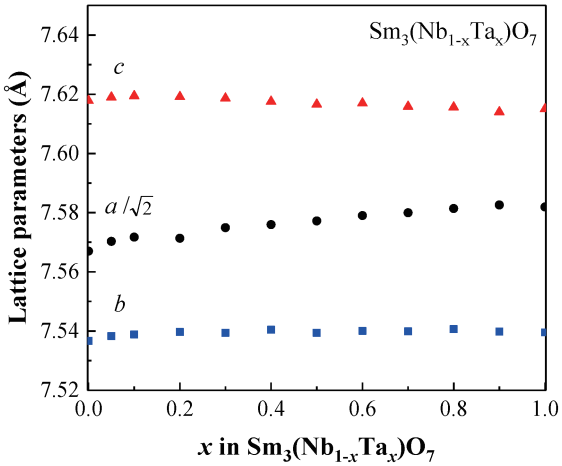

Fig. 1. Variation of lattice parameters for $Sm_3(Nb_{1-x}Ta_x)O_7$ with the ratio of Ta (x value).

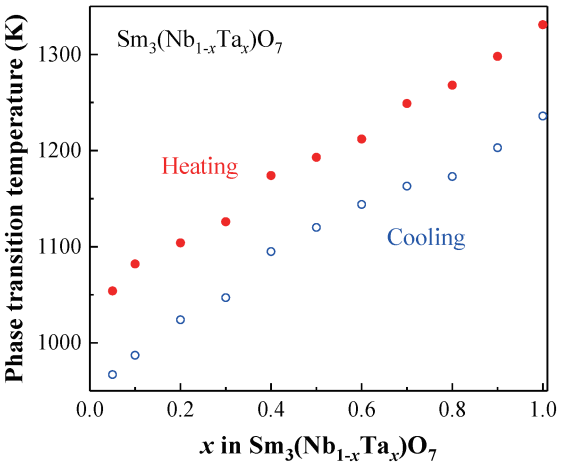

Fig. 2. Variation of phase transition temperatures for $Sm_3(Nb_{1-x}Ta_x)O_7$ with the ratio of Ta (x value).

Sm_3NbO_7 and Sm_3TaO_7 form complete solid solutions, and that their X-ray diffraction profiles are well described with the space group $C222_1$. **Figure 1** shows the variation of lattice parameters for $Sm_3(Nb_{1-x}Ta_x)O_7$ with x value. With increasing the ratio of Ta (x value), the lattice parameter a increases. On the other hand, the lattice parameters b and c are almost constant for the change of x value.

Sm_3NbO_7 undergoes the phase transition when the temperature is increased through ca. 1080 K. We performed DTA measurements for $Sm_3(Nb_{1-x}Ta_x)O_7$ ($x = 0.1$, 0.2, —, 0.9, 1.0) solid solutions in the temperature range between 298 and 1273 K. As shown in **Fig. 2**, the phase transition temperature increases with increasing the ratio of Ta (x value), and Sm_3TaO_7 undergoes the phase transition at 1340 K. **Figures 3**(a) and 3(b) show the high-temperature X-ray diffraction profiles of Sm_3TaO_7 measured at 1073 and 1473 K, respectively. The profile measured at 1073 K could be well analyzed with the Rietveld method by assuming the same space group $C222_1$ as that at room temperature. With increasing temperature, some diffraction lines which could not be indexed with space group $C222_1$ appear [for example, the diffraction lines

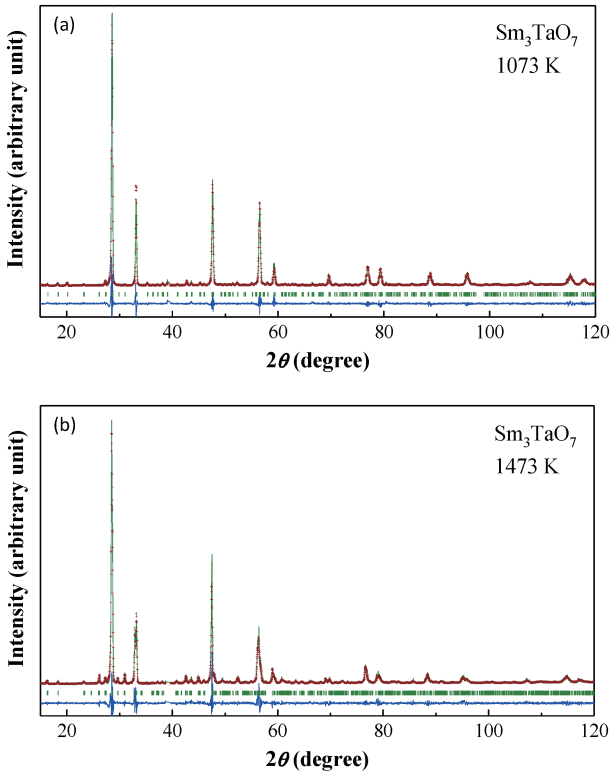

Fig. 3. Powder X-ray diffraction profiles for Sm_3TaO_7 measured at (a) 1073 K and (b) 1473 K. The calculated profiles are shown on the top solid line. The vertical marks in the middle show positions calculated for Bragg reflections. The lower trace is a plot of the difference between calculated and observed intensities. Diffraction data $2\theta = 39.14$–$39.47°$ which are ascribed to Pt heater were deleted from the Rietveld analysis.

$2\theta = 26.18$, 29.70, 31.02° corresponding to the (2 0 1), (1 3 1), and (1 2 2) reflections, respectively, see Fig. 3(b)]. At the same time, some diffraction lines disappear from the X-ray diffraction profile of Sm_3TaO_7 measured at 1073 K. They are $h0l$ reflections with odd l, for example $2\theta = 20.06$, 35.24, 38.98° corresponding to the (2 0 1), (4 0 1), and (2 0 3) reflections, respectively. Previous studies on Ln_3MO_7 (Ln = Ru, Re, Os, Ir) compounds show that above the phase transition temperature, they crystallize in the orthorhombic phase with space group *Cmcm*.[7),9),12),13),31)] We tried to analyze the X-ray diffraction profile measured at 1473 K first with the space group *Cmcm*. However, the diffraction lines could not be indexed based on the *C*-centered conditions. Then, the X-ray diffraction profiles were analyzed with the space group *Pnma*. The general reflection conditions of *Pnma* are $k + l = 2n$ for $0kl$ reflections and $h = 2n$ for $hk0$ reflections. All the reflections observed could be successfully indexed. This space group *Pnma* is the same as that for the high-temperature phase of Ln_3MoO_7 compounds.[43)] Space groups *Pnma* and $C222_1$ are both subgroup of *Cmcm*. **Table 1** lists the lattice parameters and atomic coordinates for Sm_3TaO_7 at 1073 and 1473 K.

Figures 4(a) and 4(b) illustrate the crystal structures of Sm_3TaO_7 at 1073 K ($C222_1$) and at 1473 K (*Pnma*), respectively. Both the structures have similar features: two kinds of infinite chains formed by corner-sharing TaO_6 octahedra and edge-sharing $Sm(1)O_8$ cubes, the slabs consisting of alternate chains, and 7-coordinated Sm(2)

Table 1. Structural parameters for Sm_3TaO_7

At 1073 K.

Atom	Site	x	y	z	B/Å^{2} [a]
Sm(1)	4*b*	0	0.5026(34)	1/4	0.49(3)
Sm(2)	8*c*	0.2338(2)	0.2349(2)	−0.003(1)	0.49
Ta	4*b*	0	0.9992(9)	1/4	0.51(8)
O(1)	8*c*	0.127(4)	0.185(4)	0.292(4)	0.69(7)
O(2)	8*c*	0.110(3)	0.790(4)	0.276(4)	0.69
O(3)	4*a*	0.145(1)	1/2	0	0.69
O(4)	4*a*	0.155(2)	1/2	1/2	0.69
O(5)	4*a*	0.071(3)	0	0	0.69

Note. Space group $C222_1$; $a = 10.7818(4)$ Å, $b = 7.6197(3)$ Å, $c = 7.6556(3)$ Å, $V = 628.94(4)$ Å^3, $R_{wp} = 13.39\%$, $R_I = 3.94\%$, and $R_e = 9.81\%$, where $R_{wp} = \left\{ \sum_i w_i[y_i - f_i(x)]^2 / \sum_i w_i y_i^2 \right\}^{1/2}$, $R_I = \sum |I_k(o) - I_k(c)| / \sum I_k(o)$, and $R_e = \left[(N - P) / \sum_i w_i y_i^2 \right]^{1/2}$.

a: For the same ions, B values were fixed to be equal.

At 1473 K.

Atom	Site	x	y	z	B/Å^{2} [a]
Sm(1)	4*c*	0.9909(3)	1/4	0.7345(15)	1.54(9)
Sm(2)	8*d*	0.2497(20)	0.4812(3)	0.4638(4)	1.54
Ta	4*c*	−0.0003(6)	1/4	0.2467(13)	0.60(12)
O(1)	8*d*	0.956(8)	0.356(5)	0.453(7)	0.76(20)
O(2)	8*d*	0.985(8)	0.869(4)	0.940(6)	0.76
O(3)	8*d*	0.254(17)	0.399(3)	0.719(4)	0.76
O(4)	4*c*	0.210(9)	1/4	0.306(5)	0.76

Note. Space group *Pnma*; $a = 7.6514(5)$ Å, $b = 10.8663(7)$ Å, $c = 7.5886(6)$ Å, $V = 630.93(8)$ Å^3, $R_{wp} = 14.56\%$, $R_I = 2.92\%$, and $R_e = 8.62\%$.

a: For the same ions, B values were fixed to be equal.

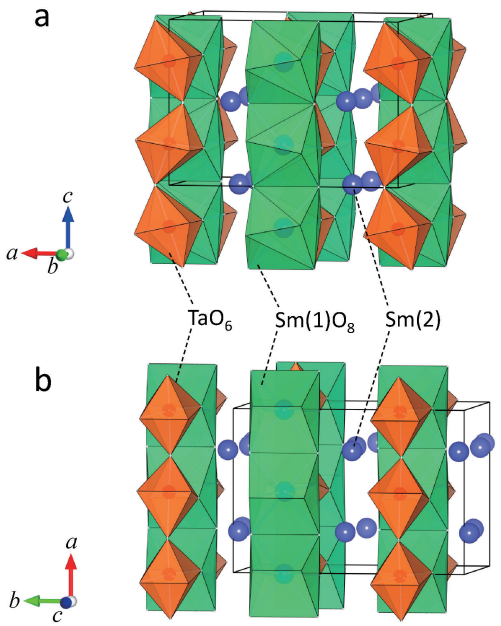

Fig. 4. Crystal structures of Sm_3TaO_7 at 1073 K (a, space group: $C222_1$) and at 1473 K (b, *Pnma*).

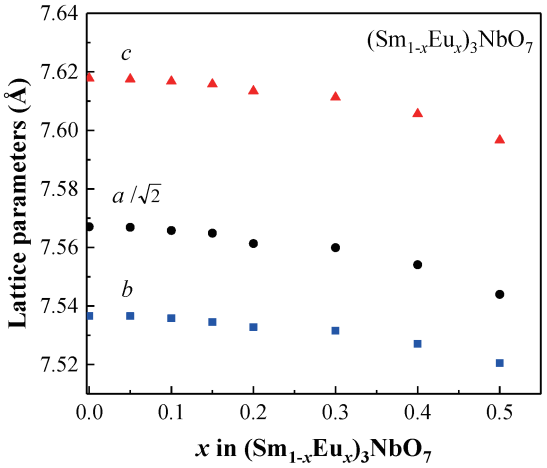

Fig. 5. Variation of lattice parameters for $(Sm_{1-x}Eu_x)_3NbO_7$ with the ratio of Eu (x value).

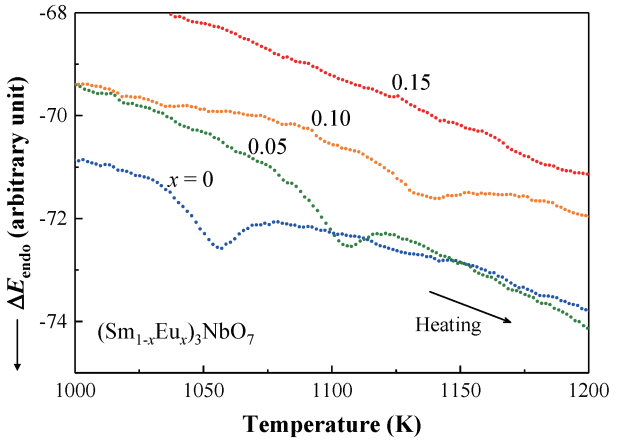

Fig. 6. DTA profiles of Sm_3NbO_7 and $(Sm_{1-x}Eu_x)_3NbO_7$ solid solutions ($x = 0.05$, 0.10, 0.15) in the temperature range between 1000 and 1200 K. The heating rate is 5 K/min.

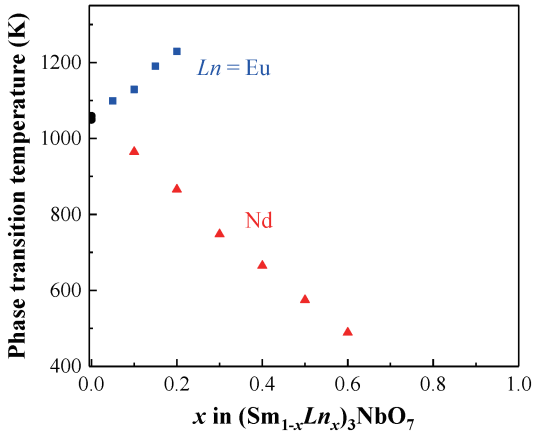

Fig. 7. Variation of phase transition temperatures for $(Sm_{1-x}Ln_x)_3NbO_7$ (*Ln* = Nd, Eu) with the ratio of *Ln* (x value).

ions exiting between the slabs. For these two structures, the TaO_6 octahedron and $Sm(1)O_6$ cube in the high temperature structure (*Pnma*) are obviously much more regular than those in the low temperature structure ($C222_1$). In the former structure [Fig. 4(b)], the TaO_6 octahedra running along the *a*-axis are tilted towards the 0 0 1 direction and the the Ta–O–Ta angle is 154.3(8)°, while in the latter structure [Fig. 4(a)], the TaO_6 octahedra running along the *c*-axis are tilted towards the 1 0 0 direction and the the Ta–O–Ta angle is 136.5(9)°.

3.2 $(Sm_{1-x}Eu_x)_3NbO_7$ solid solutions

Eu_3NbO_7 crystallizes in the orthorhombic structure with the same space group $C222_1$ as that for Sm_3NbO_7. We have prepared solid solutions $(Sm_{1-x}Eu_x)_3NbO_7$ ($x = 0.05$, 0.10, —, 0.50). The results of the X-ray diffraction measurements show that all the reflections were indexed with the space group $C222_1$. **Figure 5** shows the variation of lattice parameters for $(Sm_{1-x}Eu_x)_3NbO_7$ with x value. With increasing the ratio of Eu (x value), all the lattice parameters *a*, *b* and *c* decreases, due to the substitution of smaller Eu ions for Sm ions.

Figure 6 shows the DTA profiles for $(Sm_{1-x}Eu_x)_3NbO_7$ solid solutions in the temperature range between 1000 and 1200 K. With increasing the ratio of Eu (x value), the phase transition temperature increases, and no peak for endothermic reaction was observed for $x \geq 0.25$. **Figure 7** shows the variation of the phase transition temperature for $(Sm_{1-x}Ln_x)_3NbO_7$ (*Ln* = Nd, Eu) solid solutions against the ratio of *Ln* (x value). The DTA measurements for $(Sm_{0.8}Eu_{0.2})_3NbO_7$ solid solution show that the phase transition occurs when the temperature is increased through ca. 1250 K. Then, we carried out the high-temperature X-ray diffraction measurements between 973 and 1473 K in order to determine the crystal structure below and above the phase transition temperature. **Figures 8**(a) and 8(b) show the X-ray diffraction profiles for $(Sm_{0.8}Eu_{0.2})_3NbO_7$ measured at 973 and 1473 K, respectively. The profile measured at 973 K could be well analyzed with the Rietveld method by assuming the same space group as that at room temperature, i.e., $C222_1$. With increasing temperature, some diffraction lines which could not be indexed with space group $C222_1$ appear. As shown in Fig. 8, the X-ray diffraction profiles measured at 1473 K are more complicated than those measured at 973 K. A large number of weak reflections, forbidden for a *C*-lattice, were observed. By contrast, all the reflections are allowed for the general reflections conditions of *Pnma*, which are $k + l = 2n$ for $0kl$ reflections and $h = 2n$ for $hk0$ reflections. We adopted the *Pnma* model for the structural analyzes. The lattice parameters and atomic coordinates determined for $(Sm_{0.8}Eu_{0.2})_3NbO_7$ at 973 and 1473 K are listed in **Table 2**.

3.3 $(Sm_{1-x}Nd_x)_3NbO_7$ solid solutions

Next, we will discuss the results for $(Sm_{1-x}Nd_x)_3NbO_7$ solid solutions ($x = 0.1$, 0.2, —, 0.9). Since the crystal structure for Nd_3NbO_7 is different from that for Sm_3NbO_7 (i.e., the space groups for Nd_3NbO_7 and Sm_3NbO_7 are *Pnma* and $C222_1$, respectively[44]) at room temperature, complete solid solutions are not formed. We have analyzed the X-ray diffraction profiles for $(Sm_{1-x}Nd_x)_3NbO_7$, and

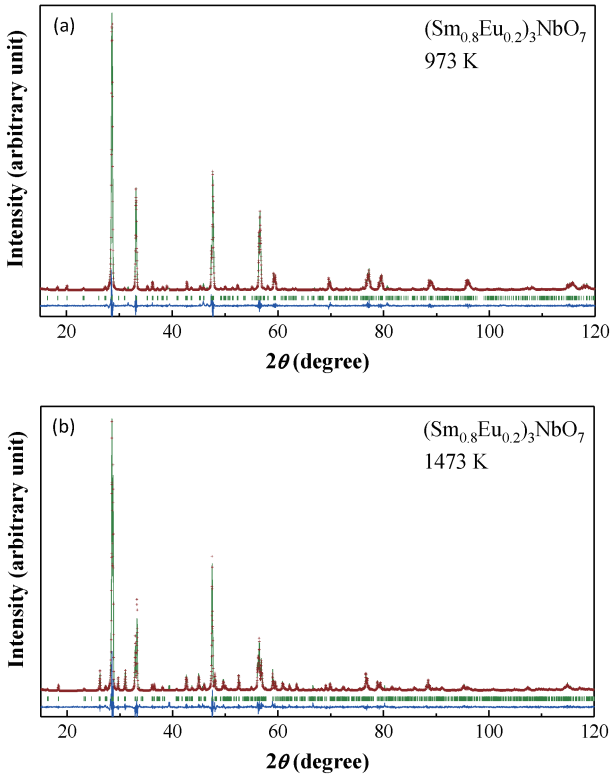

Fig. 8. Powder X-ray diffraction profiles for $(Sm_{0.8}Eu_{0.2})_3NbO_7$ measured at (a) 973 K and (b) 1473 K. The calculated profiles are shown on the top solid line. The vertical marks in the middle show positions calculated for Bragg reflections. The lower trace is a plot of the difference between calculated and observed intensities. Diffraction data $2\theta = 39.14$–$39.47°$ were deleted from the Rietveld analysis.

Table 2. Structural parameters for $(Sm_{0.8}Eu_{0.2})_3NbO_7$

At 973 K.

Atom	Site	x	y	z	B/Å^2 [a]
$Sm_{0.8}Eu_{0.2}$(1)	4*b*	0	0.4897(13)	1/4	1.19(15)
$Sm_{0.8}Eu_{0.2}$(2)	8*c*	0.2339(2)	0.2359(3)	−0.004(8)	1.19
Nb	4*b*	0	0.9992(9)	1/4	0.62(16)
O(1)	8*c*	0.122(4)	0.185(4)	0.280(4)	0.94(30)
O(2)	8*c*	0.114(3)	0.793(4)	0.293(4)	0.94
O(3)	4*a*	0.134(1)	1/2	0	0.94
O(4)	4*a*	0.131(2)	1/2	1/2	0.94
O(5)	4*a*	0.062(3)	0	0	0.94

Note. Space group $C222_1$; $a = 10.7488(3)$ Å, $b = 7.6036(2)$ Å, $c = 7.6521(2)$ Å, $V = 625.40(3)$ Å^3, $R_{wp} = 11.50\%$, $R_I = 3.94\%$, and $R_e = 9.81\%$.

a: For the same ions, B values were fixed to be equal.

At 1473 K.

Atom	Site	x	y	z	B/Å^2 [a]
$Sm_{0.8}Eu_{0.2}$(1)	4*c*	0.9927(3)	1/4	0.7439(13)	1.78(5)
$Sm_{0.8}Eu_{0.2}$(2)	8*d*	0.2494(1)	0.4815(2)	0.4611(3)	1.78
Nb	4*c*	0.0026(17)	1/4	0.2415(18)	1.27(14)
O(1)	8*d*	0.984(4)	0.350(3)	0.463(4)	1.30(30)
O(2)	8*d*	0.956(2)	0.876(3)	0.940(4)	1.30
O(3)	8*d*	0.245(7)	0.394(12)	0.725(3)	1.30
O(4)	4*c*	0.200(6)	1/4	0.307(3)	1.30

Note. Space group *Pnma*; $a = 7.6451(2)$ Å, $b = 10.8612(4)$ Å, $c = 7.5613(3)$ Å, $V = 627.85(4)$ Å^3, $R_{wp} = 13.31\%$, $R_I = 2.82\%$, and $R_e = 8.62\%$.

a: For the same ions, B values were fixed to be equal.

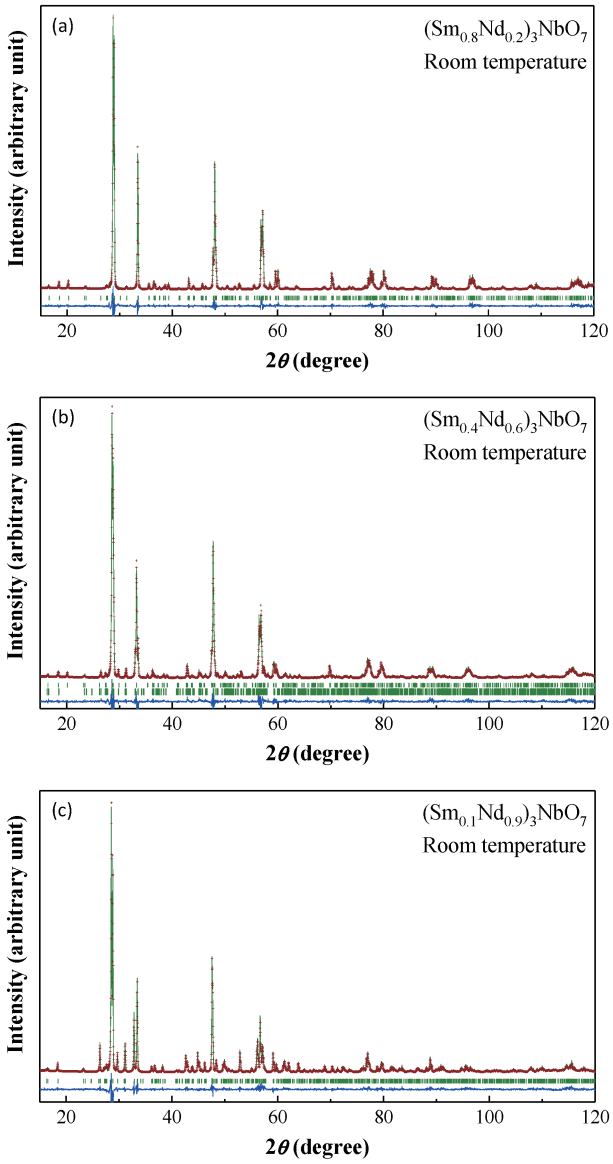

Fig. 9. Powder X-ray diffraction profiles for (a) $(Sm_{0.8}Nd_{0.2})_3NbO_7$, (b) $(Sm_{0.4}Nd_{0.6})_3NbO_7$, and (c) $(Sm_{0.1}Nd_{0.9})_3NbO_7$. The calculated profiles are shown on the top solid line. The vertical marks in the middle show positions calculated for Bragg reflections. The lower trace is a plot of the difference between calculated and observed intensities.

found that single-phase solid solutions with space group $C222_1$ and *Pnma* are formed for $x = 0.1$–0.5 and $x = 0.9$, respectively. For $x = 0.6$–0.8, the $C222_1$ and *Pnma* phases coexist. **Figure 9** shows the X-ray diffraction profiles for (a) $(Sm_{0.8}Nd_{0.2})_3NbO_7$, (b) $(Sm_{0.4}Nd_{0.6})_3NbO_7$, and (c) $(Sm_{0.1}Nd_{0.9})_3NbO_7$. **Figure 10** shows the variation of lattice parameters for $(Sm_{1-x}Nd_x)_3NbO_7$ with x value. With increasing the ratio of Nd (x value), all the lattice parameters a, b and c increase, which is due to the substitution of larger Nd ions for Sm ions.

We performed DTA measurements for all the solid solutions $(Sm_{1-x}Nd_x)_3NbO_7$ ($0.1 \le x \le 0.9$) in the temperature range between 298 and 1273 K. **Figure 11** shows the DTA profiles for $(Sm_{1-x}Nd_x)_3NbO_7$ solid solutions ($x = 0.1$–

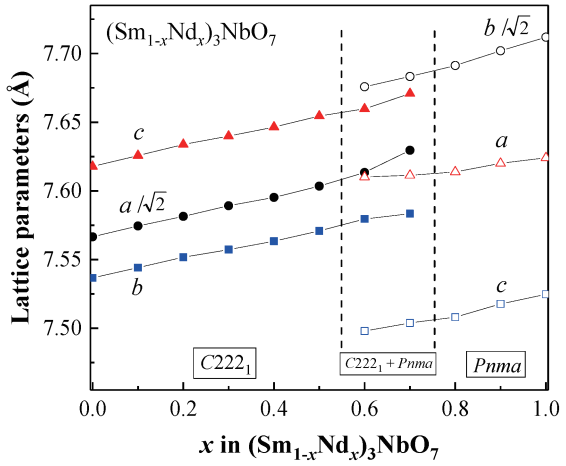

Fig. 10. Variation of lattice parameters for $(Sm_{1-x}Nd_x)_3NbO_7$ with the ratio of Nd (*x* value). Closed symbols are for $C222_1$ phase and open symbols are for *Pnma* phase.

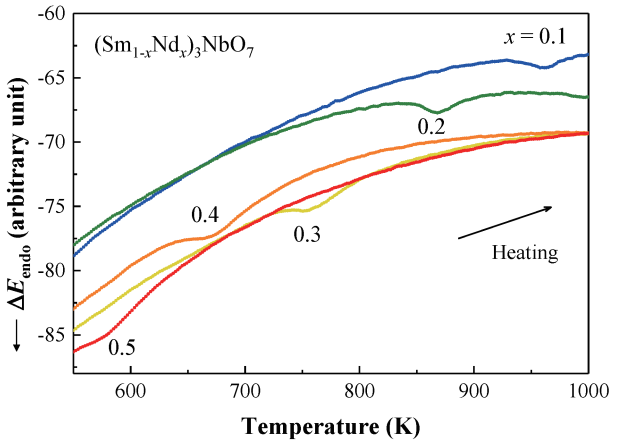

Fig. 11. DTA profiles of $(Sm_{1-x}Nd_x)_3NbO_7$ solid solutions (*x* = 0.1, 0.2, 0.3, 0.4, 0.5) in the temperature range between 500 and 1000 K. The heating rate is 5 K/min.

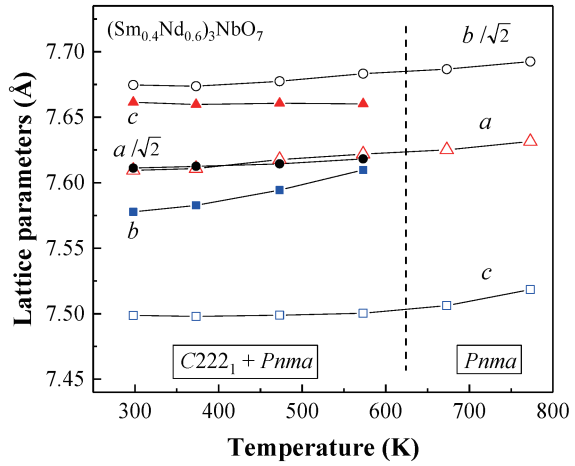

Fig. 12. Variation of lattice parameters for $(Sm_{0.4}Nd_{0.6})_3NbO_7$ with temperature in the temperature range between 295 and 773 K. Closed symbols are for $C222_1$ phase and open symbols are for *Pnma* phase.

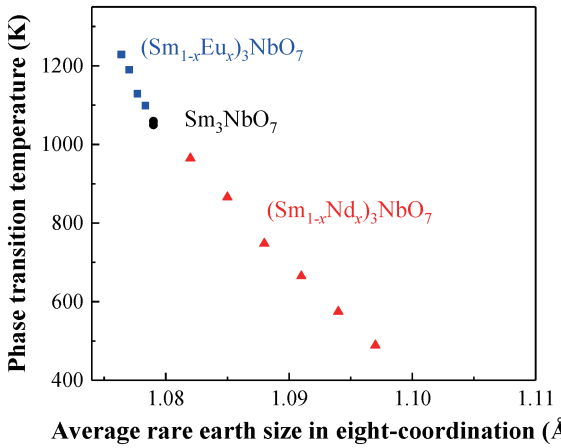

Fig. 13. Variation of phase transition temperatures for $(Sm_{1-x}Ln_x)_3NbO_7$ (*Ln* = Nd, Eu) against average rare earth size in eight-coordination.

0.5). With increasing the ratio of Nd (*x* value), the phase transition temperature decreases, which is contrastive with the results observed for $(Sm_{1-x}Eu_x)_3NbO_7$ solid solutions. The variation of the phase transition temperature against the ratio of Nd (*x* value) for $(Sm_{1-x}Nd_x)_3NbO_7$ solid solutions is also shown in Fig. 7. With increasing the ratio of Nd, the volume of $(Sm_{1-x}Nd_x)_3NbO_7$ solid solutions increases. On the other hand, that of $(Sm_{1-x}Eu_x)_3NbO_7$ solid solutions decreases with increasing the ratio of Eu. Therefore, although the variation of the phase transition temperature for $(Sm_{1-x}Ln_x)_3NbO_7$ solid solutions against *x* is opposite between *Ln* = Nd and Eu, the variation of the transition temperature against the volume shows the same trend between them, which will be discussed later (see **Fig. 13**).

The results for X-ray diffraction measurements of $(Sm_{0.4}Nd_{0.6})_3NbO_7$ show that there exist two phases, i.e., the $C222_1$ phase and the *Pnma* phase. We performed high-temperature X-ray diffraction measurements for $(Sm_{0.4}Nd_{0.6})_3NbO_7$ in the temperature range between 373 and 773 K. The Rietveld analysis for the profiles measured at 373 K indicates that the ratio of the $C222_1$ phase and the *Pnma* phase is 67.9%:32.1%. With increasing temperature, the ratio of the $C222_1$ phase decreases (53.3 and 7.5% at 473 and 573 K, respectively) and when the temperature is increased up to 673 K, all the X-ray diffraction reflections due to the $C222_1$ phase disappear, i.e., $(Sm_{0.4}Nd_{0.6})_3NbO_7$ is a single-phase solid solution with space group *Pnma*.

Figure 12 shows the variation of the lattice parameters for $(Sm_{0.4}Nd_{0.6})_3NbO_7$ with temperature in the temperature range between 295 and 773 K. The lattice parameters increase with temperature.

As shown in Fig. 7, the phase transition temperature for $(Sm_{1-x}Nd_x)_3NbO_7$ decreases with the ratio of Nd content (*x* value). On the other hand, that for $(Sm_{1-x}Eu_x)_3NbO_7$ increases with the ratio of Eu content (*x* value). Figure 13 depicts the variation of the phase transition for $(Sm_{1-x}Ln_x)_3NbO_7$ (*Ln* = Nd, Eu) against average rare earth size in eight-coordination. Both the solid solutions show the same trend, i.e., with decreasing average rare

earth size, the phase transition temperature of $(Sm_{1-x}Ln_x)_3NbO_7$ increases. This trend is the same as that for Ln_3MO_7 (M = Mo, Ru, Re, Os, or Ir). That is, the phase transition occurs with lattice contraction.

4. Summary

Sm_3NbO_7 and Sm_3TaO_7 form complete solid solutions, and their structures are well described with the space group $C222_1$. The phase transition temperature for $Sm_3(Nb_{1-x}Ta_x)O_7$ increases from 1080 K with increasing Ta concentration up to 1340 K. The phase transition temperature for $(Sm_{1-x}Nd_x)_3NbO_7$ decreases with Nd concentration. On the other hand, that for $(Sm_{1-x}Eu_x)_3NbO_7$ increases with Eu concentration. Both these solid solutions show the same trend, i.e., with decreasing average rare earth size, the phase transition temperature of $(Sm_{1-x}Ln_x)_3NbO_7$ (Ln = Nd, Eu) increases.

References

1) P. Khalifah, R. W. Erwin, J. W. Lynn, Q. Huang, B. Batlogg and R. J. Cava, *Phys. Rev. B*, **60**, 9573–9578 (1999).
2) F. Wiss, N. P. Raju, A. S. Wills and J. E. Greedan, *Int. J. Inorg. Mater.*, **2**, 53–59 (2000).
3) D. Harada and Y. Hinatsu, *J. Solid State Chem.*, **158**, 245–253 (2001).
4) D. Harada, Y. Hinatsu and Y. Ishii, *J. Phys.-Condens. Mat.*, **13**, 10825–10836 (2001).
5) D. Harada and Y. Hinatsu, *J. Solid State Chem.*, **164**, 163–168 (2002).
6) R. Lam, F. Wiss and J. E. Greedan, *J. Solid State Chem.*, **167**, 182–187 (2002).
7) W. R. Gemmill, M. D. Smith and H.-C. zur Loye, *Inorg. Chem.*, **43**, 4254–4261 (2004).
8) R. Lam, T. Langet and J. E. Greedan, *J. Solid State Chem.*, **171**, 317–323 (2002).
9) Y. Hinatsu, M. Wakeshima, N. Kawabuchi and N. Taira, *J. Alloy. Compd.*, **374**, 79–83 (2004).
10) M. Wakeshima and Y. Hinatsu, *J. Solid State Chem.*, **179**, 3575–3581 (2006).
11) J. R. Plaisier, R. J. Drost and D. J. W. IJdo, *J. Solid State Chem.*, **169**, 189–198 (2002).
12) W. R. Gemmill, M. D. Smith, Y. A. Mozharivsky, G. J. Miller and H.-C. zur Loye, *Inorg. Chem.*, **44**, 7047–7055 (2005).
13) Y. Hinatsu and Y. Doi, *J. Solid State Chem.*, **198**, 176–185 (2013).
14) R. Morrow, M. A. Susner, M. D. Sumption and P. M. Woodward, *Phys. Rev. B*, **92**, 134402 (2015).
15) H. Nishimine, M. Wakeshima and Y. Hinatsu, *J. Solid State Chem.*, **177**, 739–744 (2004).
16) Y. Hinatsu, Y. Doi, H. Nishimine, M. Wakeshima and M. Sato, *J. Alloy. Compd.*, **488**, 541–545 (2009).
17) M. Wakeshima, D. Harada and Y. Hinatsu, *J. Alloy. Compd.*, **287**, 130–136 (1999).
18) J. E. Greedan, N. P. Raju, A. Wegner, P. Gougeon and J. Padiou, *J. Solid State Chem.*, **129**, 320–327 (1997).
19) H. Nishimine, M. Wakeshima and Y. Hinatsu, *J. Solid State Chem.*, **178**, 1221–1229 (2005).
20) Y. Doi, M. Wakeshima and Y. Hinatsu, *J. Mater. Chem.*, **11**, 3135–3140 (2001).
21) L. Cai and J. C. Nino, *J. Eur. Ceram. Soc.*, **27**, 3971–3976 (2007).
22) L. Cai and J. C. Nino, *J. Eur. Ceram. Soc.*, **30**, 307–313 (2010).
23) R. Abe, M. Higashi, Z. G. Zou, K. Sayama, Y. Abe and H. Arakawa, *J. Phys. Chem. B*, **108**, 811–814 (2004).
24) R. Abe, M. Higashi, K. Sayama, Y. Abe and H. Sugihara, *J. Phys. Chem. B*, **110**, 2219–2226 (2006).
25) H. J. Rossell, *J. Solid State Chem.*, **27**, 115–122 (1979).
26) A. Kahn-Harari, L. Mazerrolles, D. Michel and F. Robert, *J. Solid State Chem.*, **116**, 103–106 (1995).
27) F. P. F. van Berkel and D. J. W. IJdo, *Mater. Res. Bull.*, **21**, 1103–1106 (1986).
28) W. A. Groen, F. P. F. van Berkel and D. J. W. IJdo, *Acta Crystallogr. Sec. C*, **43**, 2262–2264 (1986).
29) N. Ishizawa, K. Tateishi, S. Kondo and T. Suwa, *Inorg. Chem.*, **47**, 558–566 (2008).
30) G. Wltschek, H. Paulus, I. Svoboda, H. Ehrenberg and H. Fuess, *J. Solid State Chem.*, **125**, 1–4 (1996).
31) Y. Hinatsu and Y. Doi, *J. Solid State Chem.*, **220**, 22–27 (2014).
32) Y. Yokogawa, M. Yoshimura and S. Somiya, *Mater. Res. Bull.*, **22**, 1449–1456 (1987).
33) Y. Yokogawa, M. Yoshimura and S. Somiya, *Solid State Ionics*, **28**, 1250–1253 (1988).
34) J. F. Vente, R. B. Helmholdt and D. J. W. IJdo, *J. Solid State Chem.*, **108**, 18–23 (1994).
35) M. Wakeshima, H. Nishimine and Y. Hinatsu, *J. Phys.-Condens. Mat.*, **16**, 4103–4120 (2004).
36) J. F. Vente and D. J. W. IJdo, *Mater. Res. Bull.*, **26**, 1255–1262 (1991).
37) M. Inabayashi, Y. Doi, M. Wakeshima and Y. Hinatsu, *J. Solid State Chem.*, **250**, 100–106 (2017).
38) M. Inabayashi, Y. Doi, M. Wakeshima and Y. Hinatsu, *J. Solid State Chem.*, **254**, 150–154 (2017).
39) Y. Hinatsu and Y. Doi, *J. Solid State Chem.*, **182**, 1694–1699 (2009).
40) Y. Hinatsu and Y. Doi, *J. Solid State Chem.*, **217**, 16–21 (2014).
41) N. Barrier and P. Gougen, *Acta Crystallogr. E*, **59**, i22–i24 (2003).
42) N. Barrier and P. Gougen, *Acta Crystallogr. C*, **63**, i102–i104 (2003).
43) M. Wakeshima and Y. Hinatsu, *J. Solid State Chem.*, **183**, 2681–2688 (2010).
44) Y. Doi, Y. Harada and Y. Hinatsu, *J. Solid State Chem.*, **182**, 709–715 (2009).
45) A. N. Klimenko, Y. S. Kozlov, V. S. Sergeev and E. A. Pastukhov, *Thermochim. Acta*, **209**, 331-338 (1992).
46) L. Cai, S. Denev, V. Gopalan and J. C. Nino, *J. Am. Ceram. Soc.*, **93**, 875–880 (2010).
47) L. Cai, S. Denev, V. Gopalan and J. C. Nino, *J. Solid State Chem.*, **184**, 2263–2271 (2011).
48) Y. Hinatsu and Y. Doi, *Solid State Sci.*, **68**, 19–24 (2017).
49) F. Izumi and K. Momma, *Solid State Phenom.*, **130**, 15–20 (2007).
50) K. Momma and F. Izumi, *J. Appl. Crystallogr.*, **41**, 653–658 (2008).